

Smartphone Imaging Flow Cytometry for High-Throughput Single-Cell Analysis

Mahmut Kamil Aslan, Yun Ding, Stavros Stavrakis,* and Andrew J. deMello*



Cite This: *Anal. Chem.* 2023, 95, 14526–14532



Read Online

ACCESS |



Metrics & More

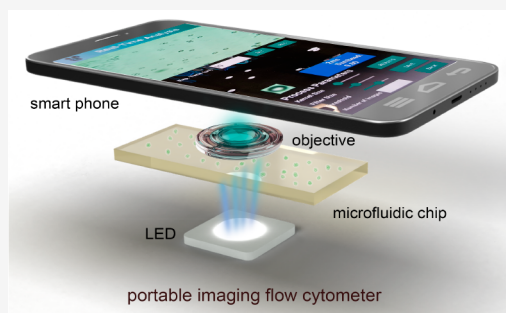


Article Recommendations



Supporting Information

ABSTRACT: We present a portable imaging flow cytometer comprising a smartphone, a small-footprint optical framework, and a PDMS-based microfluidic device. Flow cytometric analysis is performed in a sheathless manner via elasto-inertial focusing with a custom-written Android program, integrating a graphical user interface (GUI) that provides a high degree of user control over image acquisition. The proposed system offers two different operational modes. First, “post-processing” mode enables particle/cell sizing at throughputs of up to 67 000 particles/s. Alternatively, “real-time” mode allows for integrated cell/particle classification with machine learning at throughputs of 100 particles/s. To showcase the efficacy of our platform, polystyrene particles are accurately enumerated within heterogeneous populations using the post-processing mode. In real-time mode, an open-source machine learning algorithm is deployed within a custom-developed Android application to classify samples containing cells of similar size but with different morphologies. The flow cytometer can extract high-resolution bright-field images with a spatial resolution <700 nm using the developed machine learning-based algorithm, achieving classification accuracies of 97% and 93% for Jurkat and EL4 cells, respectively. Our results confirm that the smartphone imaging flow cytometer (sIFC) is capable of both enumerating single particles in flow and identifying morphological features with high resolution and minimal hardware.



INTRODUCTION

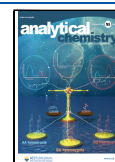
Flow cytometry is a ubiquitous analytical technique for enumerating and detecting cells suspended in a flowing stream. It remains the gold standard method for counting and identifying cells within large heterogeneous populations due to its quantitative nature and its ability to operate at high throughputs (>10 000 cells/s).¹ A conventional flow cytometer integrates a hydrodynamic system (almost always incorporating a sheath fluid) that focuses cells into a single-file stream and an optical detection system (accompanied by a signal-processing system) that is able to extract information relating to the size, morphology, and content of the individual cells.² Such a platform allows for high-throughput cell enumeration, with the analytical throughput being controlled by both the sample concentration and the flow rate.^{3,4} Although conventional flow cytometers are able to collect scattering and fluorescence signals, they do not provide high-quality morphological information relating to complex cellular phenotypes.⁵ Additionally, conventional flow cytometers are bulky and expensive and normally have to be operated by a trained specialist in a central facility. All of these characteristics limit the use of flow cytometry in resource-limited regions⁶ and in point-of-care (POC) diagnostics applications. Imaging flow cytometry (IFC) is a variant of flow cytometry that allows for the high-throughput imaging of cellular populations. IFC combines the high-throughput nature of conventional flow cytometry with the enhanced sensitivity and imaging

capabilities of optical microscopy and, therefore, provides for significant improvements in both the information content and information retrieval rates.⁷ Unfortunately, the analytical throughput of commercial imaging flow cytometers is typically limited to 5000 cells/s at 20× magnification or 2000 cells/s at 40× magnification.⁸ This is approximately 1 order magnitude lower than the maximum throughputs reported for conventional flow cytometers. Fortunately, recent efforts have leveraged the capabilities of microfluidic-based imaging flow cytometers, providing significantly higher throughputs. For example, Rane et al. reported an imaging flow cytometer based on inertial focusing that was able to generate fluorescence images of single cells at a throughput of 96 000 cells/s.⁹ In this study, stroboscopic illumination was used to extract multicolor fluorescence, bright-field, and dark-field images of cells and to perform accurate cell sizing and cell cycle analysis in heterogeneous populations. In a related work, Goda and colleagues demonstrated the acquisition of fluorescence images of human cancer cells moving at velocities of 1 m/s using light-

Received: July 21, 2023

Accepted: September 7, 2023

Published: September 21, 2023



sheet excitation within a mirror-embedded microfluidic device.¹⁰ This platform afforded an analytical throughput of 10 000 cells/s, with offline image-based classification of MCF-7 (human breast adenocarcinoma) and HT-29 (human colorectal adenocarcinoma) cells successfully extracting morphological features, such as cell area and cell perimeter. Additionally, Holzner and co-workers presented an ultra-high-throughput imaging flow cytometer by incorporating elasto-inertial cell focusing and multiparametric detection.¹¹ This platform, which again used stroboscopic illumination, enabled bright-field and multicolor fluorescence analysis of subcellular structures down to 500 nm and at rates in excess of 60 000 cells/s. Although the aforementioned studies provide imaging information at high analytical throughputs, they require the use of microscopes and sophisticated optical components, such as acousto-optic tunable filters, high numerical aperture objectives, and high-speed cameras. To address this issue, Ottesteanu et al. recently reported a more compact, low-cost imaging flow cytometer incorporating offline deep learning for blood diagnostics.¹² The instrument, consisting of a simple (elasto-inertial) microfluidic cytometer, a custom-built optical unit, and a low-cost camera, was successfully used to perform morphology-based clinical diagnosis of Sézary syndrome. While simple to implement, the platform was limited to single-cell analysis at rates of up to 500 cells/s.

According to Statista,¹³ there are currently over 6.8 billion smartphone users worldwide. Unsurprisingly, smartphones are increasingly being used in a range of wellness and healthcare applications, such as the diagnosis of skin lesions,^{14,15} the quantification of lateral flow assays,^{16–18} glucose detection,¹⁹ biomarker detection,²⁰ and general health and activity monitoring.²¹ Additionally, because of the recent advances in both hardware and software capabilities, smartphones are now being used as digital microscopes for the analysis of bodily fluids. For example, Im et al. reported a smartphone-based microscope for cancer cell diagnostics.²² In this study, target cells that were immunolabeled with molecule-specific microbeads were used to generate unique diffraction patterns that could be imaged by using a smartphone camera. The acquired images were then transferred to a server for image reconstruction and analysis. Significantly, this label-free microscopy platform was used to screen cancer cells in cervical specimens and detect human papillomavirus DNA. In related studies, smartphone images and a deep learning framework were used to screen sickle cells in blood smears.²³ Here, blood smear images that were acquired using a smartphone camera were processed using deep neural networks for the semantic segmentation of healthy and sickle cells. Importantly, this platform achieved ~98% accuracy in sickle cell detection across 96 patient samples that included 32 patients with sickle cell disease. Although the aforementioned (image cytometry) studies involved the use of compact, portable, and easy-to-use instruments, they all required laborious computational steps and were only able to analyze static cellular suspensions. This precludes their use as high-throughput and simple-to-use IFC-based platforms for point-of-care applications. Interestingly, a cell-phone-based optofluidic imaging cytometry platform integrating compact optical components was recently presented by Ozcan and co-workers.²⁴ In this platform, fluorescently labeled particles or cells of interest were continuously delivered to an imaging probe volume through a disposable microfluidic channel positioned above the camera

of a smartphone. This platform was used to measure the density of white blood cells in blood samples with an optical (spatial) resolution of approximately 2 μm . However, the volumetric flow rates were extremely low (<1 $\mu\text{L}/\text{min}$), and thus, the analytical throughputs (of ~130 cells/s) were orders of magnitude lower than the typical throughputs associated with conventional imaging flow cytometers. Consequently, there is an unmet need for a portable, easy-to-use, and high-throughput imaging flow cytometry system. To this end, we report the design, fabrication, and testing of a smartphone-based portable imaging flow cytometer (sIFC) for the enumeration of cells and particles that operates at an analytical throughput of up to 67 000 particles/s. The system consists of a single-channel microfluidic device, a smartphone, and a small number of external optical components.

The fabricated sIFC offers two distinct operational modes. First, “post-processing” mode enables particle/cell sizing in a sample with processing throughputs of up to 67 000 particles/s. Alternatively, “real-time” mode allows for integrated cell/particle classification (based on size and morphology) through machine learning at throughputs of 100 particles/s.

■ MATERIALS AND METHODS

Design and Fabrication of the Microfluidic Device.

The microfluidic device comprises a single rectangular cross-section microchannel that is 50 mm long, 1 mm wide, and 25 μm deep. Such a low aspect ratio, rectangular cross-section microchannel allows for efficient elasto-inertial focusing of cells (with a mean diameter of 12 μm) in the image plane.²⁵ The microchannel pattern was designed using the AutoCAD 2019 software (Autodesk, San Rafael, CA, USA) and was printed onto a thin-film photolithographic mask (Micro Lithography Services, Ltd., Chelmsford, UK). Standard photolithographic techniques were used to fabricate an SU-8 master mold. First, SU-8 2010 photoresist (Micro Resist Technology, Berlin, Germany) was spin-coated onto a 5 in. diameter silicon wafer (Siegert Wafer GmbH, Aachen, Germany). A spin speed of 2000 rpm resulted in a 25 μm thick resist layer. The coated wafer was baked at 65 $^{\circ}\text{C}$ for 1 min and then at 95 $^{\circ}\text{C}$ for 4 min on a hot plate. Channel patterns in the mask were transferred to the SU-8-coated wafer via ultraviolet (UV) exposure for 30 s. Subsequently, the wafer was baked on a 95 $^{\circ}\text{C}$ hot plate for 4 min to facilitate the cross-linking of the exposed SU-8 photoresist. The patterned structures were developed in an mr-Dev 600 developer solution (Micro Resist Technology, Berlin, Germany), which removes the unexposed regions of the photoresist. Finally, the wafer was thoroughly rinsed with isopropyl alcohol and water before being dried with pressurized air. The fabricated mold was then hard-baked at 150 $^{\circ}\text{C}$ on a hot plate for 10 min.

Soft lithography was used to fabricate the microfluidic devices. Briefly, the mold was placed into a desiccator containing a beaker of chlorotrimethylsilane (Sigma-Aldrich, Buchs, Switzerland) for 2 h at a pressure of 150 mbar. Mold functionalization with chlorotrimethylsilane was performed to aid the eventual peeling of the cured polydimethylsiloxane (PDMS) substrate from the mold. A PDMS mixture was then prepared using a 10:1 (w/w) ratio of PDMS base to curing agent (SYLGARD 184, Dow Corning, Midland, TX, USA). This mixture was poured onto the mold, degassed in the desiccator for 30 min, and cured overnight in an oven at 70 $^{\circ}\text{C}$. The cured PDMS was then peeled off the mold, and individual devices were formed by dicing with a scalpel. Access ports

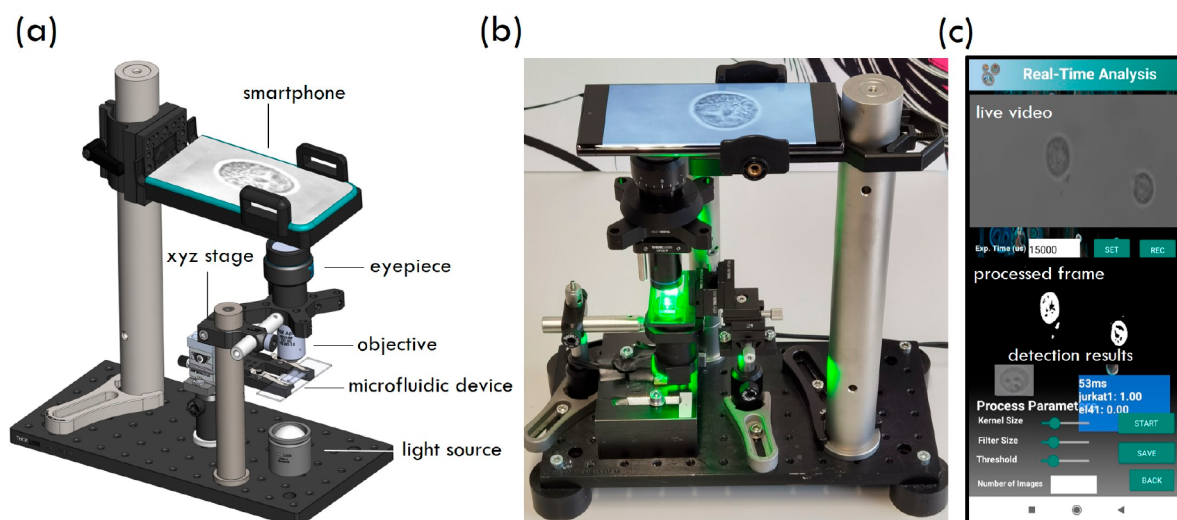


Figure 1. The smartphone imaging flow cytometer (sIFC). The sIFC platform comprises a microfluidic device, a smartphone, and a compact optical setup. (a) Schematic of the optical components within the sIFC. (b) Photograph of the sIFC. (c) The real-time analysis screen of the SmartFlow application, which displays images captured using the sIFC and the classification results of the machine learning algorithm.

(0.76 mm in diameter) were formed by using a hole puncher (Syneo, West Palm Beach, FL, USA). The devices were then bonded to glass slides (Corning, NY, USA) after exposing both surfaces to oxygen plasma using an EMITECH K1000X plasma asher (Quorum Technologies, Laughton, UK) for a period of 1 min. Finally, the bonded devices were left on a hot plate at 120 °C for 2 h to strengthen the bond.

Cell Preparation. Jurkat and mouse malignant (EL4) cells were cultured in DMEM medium (Life Technologies, Zug, Switzerland) and supplemented with Glutamax (Life Technologies, Zug, Switzerland), 10% (v/v) fetal bovine serum (FBS, Life Technologies, Zug, Switzerland), and 1% (v/v) penicillin-streptomycin (10 000 units/mL, Life Technologies, Zug, Switzerland) at 37 °C and 5% CO₂ (New Brunswick Galaxy 170 S, Eppendorf, Schönenbuch, Switzerland). All experiments were performed on cells in their exponential (log) phase of growth.

Optical Setup and Android Application. The optical setup consisted of a 10×/22 mm wide field eyepiece (Nikon 10×, Egg, Switzerland), a series of objective lenses such as a 40×/0.65 NA lens or a 60×/0.85 NA lens (AmScope, Inc., Irvine, CA, USA), a collimated light-emitting diode (LED) light source (Thorlabs GmbH, Bergkirchen, Germany), and a miniature dovetail xyz stage (Thorlabs GmbH, Bergkirchen, Germany) (Figure 1a). The microfluidic device was attached to a custom-designed aluminum holder mounted onto the dovetail stage. The camera of a Xiaomi Mi 9 cell phone (equipped with the Android 10 operating system) was used to acquire images of particles and cells in flow. The Xiaomi Mi 9 smartphone integrates a 48-megapixel RGB primary camera that is able to capture images at rates of up to 240 frames/s with an exposure time of 15 μs. The smartphone was placed within a bespoke 3D-printed case and stabilized with a pedestal pillar post (Thorlabs GmbH, Bergkirchen, Germany). The optical components were mounted and stabilized using a cage system with the optical posts mounted on an optical breadboard (all Thorlabs GmbH, Bergkirchen, Germany). An eyepiece was placed directly in front of the primary camera of the smartphone, and variable magnification factors were achieved by exchanging the objective lens. This allowed higher

spatial resolution (<0.7 μm) imaging for cell morphology analysis (Figure S1). It is useful to note that the use of external lenses such as a 10× eyepiece is beneficial in providing extra magnification, but it can also potentially cause distortion in specific regions of the image, resulting in a decreased field of view, as shown in Figure S4. Additionally, lens switching will affect the location of the focal plane to some degree. For these reasons, we have incorporated a miniaturized dovetail translation *z* stage to allow for manual image refocusing. This manual focusing system has been tested with objectives having magnifications between 4× and 60× and shown to be effective.

A custom Android application based on the TensorFlow framework (Google, Mountain View, CA, USA) was created for image analysis. The application, termed SmartFlow, integrates a graphical user interface (GUI) and works to capture raw cell images, process them in real time, and display the image classification results as probability values (Figure 1c). The Android application consists of two primary components: a main menu and a real-time analysis module. The main menu allows the user to initiate a flow cytometry experiment and to extract classification results from imaging cytometry experiments; it also provides instructions and information regarding the imaging flow cytometry application (Figure 1c). The real-time analysis screen integrates a number of features, including the real-time acquisition of cell images, the classification of results via a machine learning algorithm, and adjustments for the exposure time, kernel size, filter size, and threshold. Briefly, the kernel size defines the size (in pixels) of the square structural element used in the morphological operations, the filter size specifies the size of the median filter (in pixels) used to denoise the raw image (if required), and the threshold sets a threshold value (between 0 and 255) for the image binarization operation that is performed on the background-subtracted image. The user can also set the exposure time and initiate the real-time processing algorithm by pressing the “START” button. The raw images that are captured with the smartphone camera are processed through an image-processing pipeline that includes background subtraction, thresholding, and morphological

operations. These are described in more detail in Figure S2. Next, individual cells identified in these images are delivered to a machine learning algorithm that classifies different types of cells according to their morphological characteristics. The machine learning algorithm is based on a transfer learning technique, and the network architecture of the algorithm is described in the Supporting Information.

Microfluidic Device Operation. Suspensions of different-sized polystyrene beads (Thermo Fischer Scientific, Basel, Switzerland) and different cell lines were prepared at concentrations between 8×10^6 and 4.5×10^7 beads/mL and 4×10^6 and 6×10^6 cells/mL, respectively. Suspensions were loaded into 5 mL glass vials (Hamilton Lab Products, Reno, NV, USA) and delivered into the microfluidic device using a precision pressure pump (Dolomite Microfluidics, Royston, UK) at 500 mbar. The microfluidic device was placed on a dovetail xyz translation stage to allow positioning of the optical system in the imaging plane. Poly(ethylene oxide) (PEO) solutions were added to all particle/cell suspensions to enable cell/particle focusing in a sheathless manner. A stock solution of 1 MDa PEO (Sigma-Aldrich, Buchs, Switzerland) at a concentration of 10 000 ppm was prepared in Dulbecco's phosphate-buffered saline (DPBS; Life Technologies, Zug, Switzerland) and aged at room temperature for one month to enhance PEO stability.²⁵ The stabilized PEO solution was diluted with DPBS prior to imaging cytometry experiments, resulting in a final PEO concentration of 1000 ppm. Cell suspensions were mixed with 20% v/v Optiprep density gradient medium (Sigma-Aldrich, Buchs, Switzerland) to minimize cell sedimentation.

RESULTS AND DISCUSSION

Polymer Bead Quantitation. To assess the operational throughput of the sIFC system, initial experiments focused on the analysis of suspensions containing polystyrene beads with diameters of 10, 12, and 15 μm . The maximum accessible frame rate of the Xiaomi Mi 9 smartphone camera is 240 frames/s. Assuming a 40 \times magnification, the field of view of the imaging flow cytometer was approximately 0.5 mm \times 0.5 mm. A driving pressure of 500 mbar, which corresponds to an average bead velocity of 0.072 m/s, was used to ensure that each bead was imaged only once in each frame to avoid oversampling. Additionally, to ensure that the motion blur was <1 μm , the camera exposure time was set to 15 μs . Two different bead suspensions were then delivered into the microfluidic cytometer and imaged. Figure 2a,b shows representative raw images (left) captured by the sIFC and the same images after image processing by our custom MATLAB script (right). Size distribution histograms of the bead mixtures were then generated from the sIFC data (Figure 2c,d, left graphs) and compared to the data generated using a CytoFLEX flow cytometer (Beckman Coulter, Nyon, Switzerland) (Figure 2c,d, right graphs). It can be seen that the sIFC is able to accurately size and discriminate microparticles with a diameter difference of 2 μm (Figure 2d) at a throughput of $\sim 67\,000$ beads/s. It should be noted that the entire field of view of the system is 629.47 $\mu\text{m} \times 841.57 \mu\text{m}$. This corresponds to an analytical throughput of approximately 140 000 beads/s based on a bead concentration of 4.5×10^7 beads/mL. However, due to optical distortion, the field of view is decreased to 503.88 $\mu\text{m} \times 503.04 \mu\text{m}$, yielding a reduced throughput of 67 578 beads/s (Figure S4). This rate is approximately 20 times higher than that of conventional

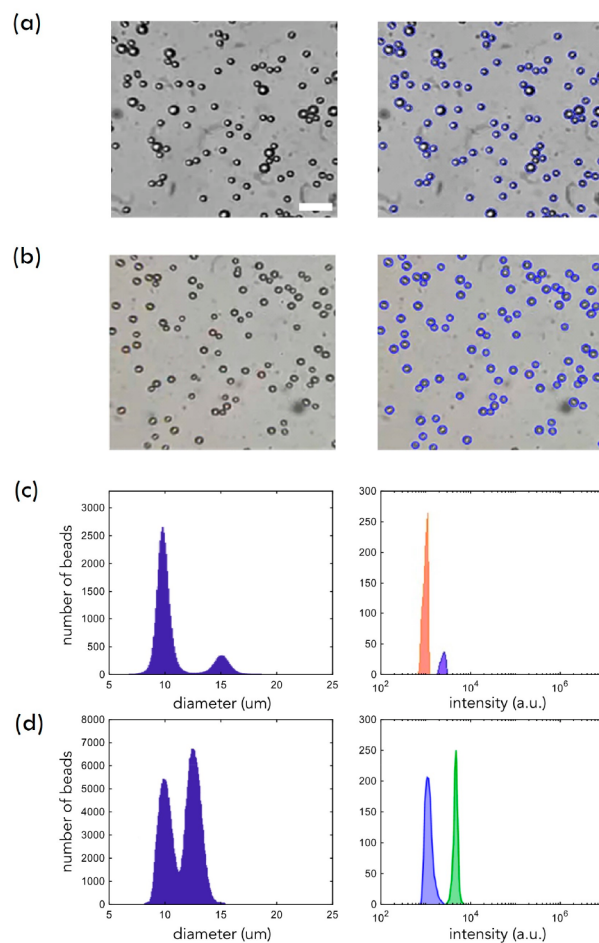


Figure 2. High-throughput particle quantification using the sIFC platform. (a) Raw (left) and processed (right) images for a bead mixture containing particles with diameters of 10 and 15 μm . (b) Raw (left) and processed (right) images of a bead mixture containing particles with diameters of 10 and 12 μm . (c, d) Size histograms obtained using the sIFC platform (left) and a high-end commercial flow cytometer (right) for the same bead mixtures as those shown in panels (a) and (b). The scale bar is 40 μm .

benchtop imaging cytometers (notably, the Cytek Amnis FlowSight). Operation at such high throughput is critical when screening rare cells, such as circulating tumor cells (CTCs). CTCs are extremely rare when compared to other cells in whole blood, being found in quantities as low as 1–10 CTCs/billion blood cells. In this regard, it is important to note that conventional flow cytometry can be used to detect CTCs; however, processing times are unacceptably long, often taking more than 24 h per sample.²⁶ In contrast, the sIFC, operating at 67 000 cells/s, dramatically reduces sample-processing times to a couple of hours.

The average size of an image file taken with the sIFC is approximately 0.6 Mb. If we assume a smartphone storage capacity of 128 Gb, over 200 000 images may be stored at any time. When using 40 \times magnification, a single image frame will contain approximately 280 particles (i.e., 67 000 particles/s \div 240 frames/s). This means that the sIFC can store approximately 5.5×10^7 particle images. System performance with regard to post-processing throughput can obviously be improved by using a laptop equipped with a cloud-connected multicore graphical processing unit (GPU) or a more portable

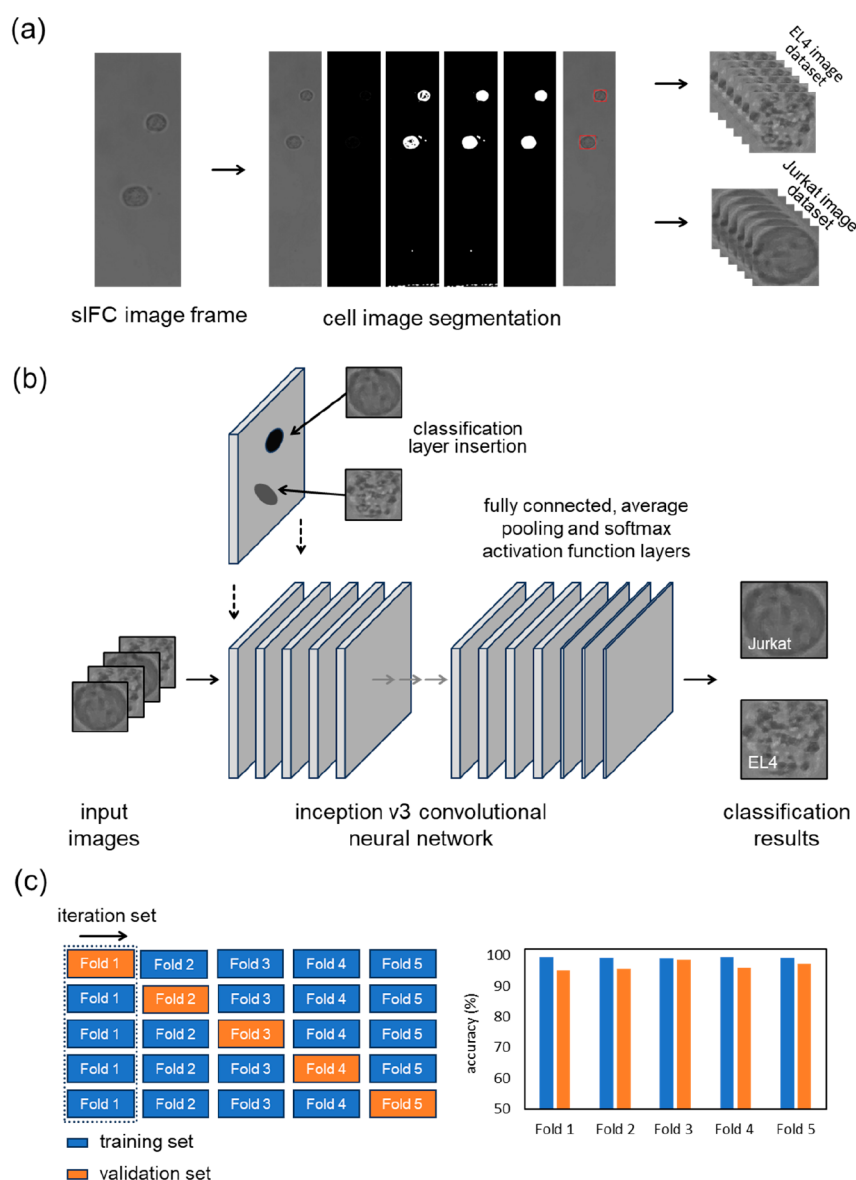


Figure 3. Machine learning algorithm workflow. (a) The algorithm workflow begins by recording images from both cell populations. Next, single EL4 and Jurkat cells are segmented using the image-processing pipeline described in Figure S2. (b) A transfer learning approach was used to generate the machine learning model for the classification of Jurkat and EL4 cells. For this purpose, the Google Inception v3 convolutional neural network was retrained using single-cell images and subsequently used to generate a customized network for Jurkat and EL4 cell classification. (c) The customized network was validated using a 5-fold cross-validation approach. This involved splitting the data set into 5 equal subsets (or folds). Then, training and validation accuracies were calculated for each fold. The mean training accuracy and validation accuracy of the 5-fold validation were 99.4 and 96.5%, respectively.

and cost-effective alternative, such as an NVIDIA Jetson development board dedicated for machine learning.

To provide a more complete assessment of the capabilities of the sIFC, it is important to account for the trade-offs between throughput and image quality. When acquiring images of rapidly moving objects, motion blur is controlled by the exposure time of the camera, with extended exposure times increasing motion blur and decreasing the image quality. In the current system, the short exposure times ($\sim 14 \mu\text{s}$) provided by the smartphone camera combined with a powerful light source ensure blur-free imaging at high cell velocities ($< 0.1 \text{ m/s}$). Motion blur can also be suppressed by modulating the illumination light. Such an upgrade would afford sensitivities equivalent to those of commercial imaging flow cytometers while also allowing for operation at an ultra-high throughput.

Machine Learning-Based Cell Classification. The sIFC platform was then used to perform machine learning-based classification of different cell populations by analyzing the distinct morphological features obtained by bright-field imaging. To build a machine learning-based cell image classifier, a pretrained Inception v3 model (Google, Mountain View, CA, USA) was retrained using images of Jurkat and EL4 cells to generate a customized model. The Inception v3 model has a simple architecture and a moderate computational cost when compared to other high-performance machine learning models. Regardless, the Inception v3 convolutional neural network provides a high cell classification efficiency, especially when considering the memory and computing power limitations associated with smartphone use.²⁷ To generate a robust model for classifying Jurkat and EL4 cells, we adopted

the transfer learning technique.²⁸ First, Jurkat and EL4 cell suspensions were driven through the microfluidic device in separate (pure) flows, with movies being recorded by the sIFC. The movies were then analyzed, with individual cells being detected using the previously described image-processing operations (Figure 3a). For each cell class (i.e., Jurkat and EL4), 3500 single-cell images were extracted and analyzed. Next, the pretrained model was retrained for each population using a transfer learning technique by inserting a customized classification layer for the EL4 and Jurkat cell data sets. The customized model consists of two output classes that are defined as “Jurkat” and “EL4”. Figure 3b illustrates the workflow associated with the developed machine learning algorithm. It is important to note that Jurkat and EL4 cells are very similar in size; however, they have different shapes and degrees of cytoplasmic granularity. Accordingly, the machine learning classifier operates primarily on the basis of morphological variations between each cell type. To validate the customized model, a 5-fold validation approach was utilized. In short, the “Jurkat” and “EL4” cell image sets were divided into 5 equal subsets, and the network was iteratively trained five times by using different training and validation sets at each iteration (Figure 3c, left panel). Then, for each set (fold), both training and validation accuracies were calculated, as shown in Figure 3c. After the 5-fold validation process, the customized model achieved a training accuracy and a validation accuracy of 99.4 and 96.5%, respectively.

To assess the accuracy of our machine learning-based classifier, the generated model was tested with different input data sets using Jurkat and EL4 cells. First, two sets of images from each cell line (where each set contained 500 images) were given as input images to the model. Significantly, the generated model correctly classified 97% and 93% of the images of Jurkat and EL4 cells, respectively (Figure 4a,b, right panels). It should be noted that the small number of incorrect classifications primarily occurred as a result of the images being out of focus (Figure S3). Subsequently, two image sets (each containing 500 images), acquired from a mixture of Jurkat and EL4 cells that was prepared at a ratio of 40:60 (Jurkat:EL4 cells), were fed into the model as input images. As previously noted, Jurkat and EL4 cells are similar in size (Figure 4a,b, left panels) and, therefore, there is a considerable overlap in the extracted size distributions. This means that it is impossible to accurately discriminate the cells within a mixed population using solely size-based classification (Figure 4c, left panel). However, the machine learning model was highly successful in correctly classifying individual cells as either Jurkat or EL4 cells within the cell mixture, as indicated by the extracted concentration percentage of each cell type shown in Figure 4c (right panel). These results are in almost perfect agreement with the input ratio of 40:60 (Jurkat:EL4 cells). The entire information extraction process, which includes image acquisition, image processing, and classification, takes approximately 10 ms. Accordingly, this yields a real-time analytical throughput of 100 cells/s.

CONCLUSIONS

To conclude, we have developed a portable, lightweight, and inexpensive smartphone-based imaging flow cytometry platform that is able to perform real-time image classification and the enumeration of single cells using machine learning. The system consists of a smartphone, a compact optical system, and a real-time cell quantification application. The SmartFlow

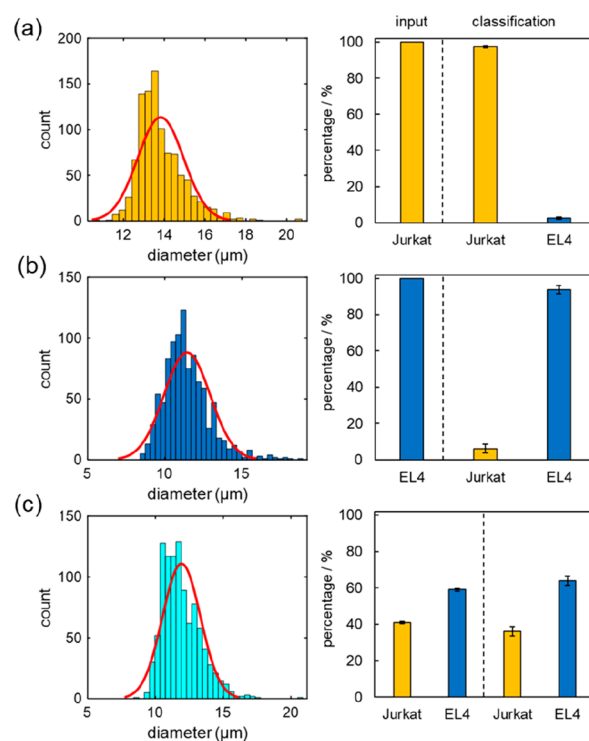


Figure 4. Machine learning-based classification. The integrated machine learning model was tested using three different image sets that originated from pure populations of Jurkat and EL4 cells and a 40:60 Jurkat:EL4 cell mixture. (a) Size distribution (left) and classification results (right) of the machine learning model for Jurkat cells. (b) Size distribution (left) and classification results (right) of the machine learning model for EL4 cells. (c) Size distribution (left) and classification results (right) of the machine learning model for a 40:60 Jurkat:EL4 cell mixture. The data indicate that Jurkat and EL4 cells could not be discriminated by size-based classification. However, machine learning classification (based on morphological features) was highly effective in distinguishing Jurkat and EL4 cells within mixed populations.

application integrates a GUI that can acquire and process bright-field images from flowing cells and display the classification results in real time. Significantly, the sIFC was able to operate at analytical throughputs of >67 000 particles/s, which represents a 20-fold improvement over high-end imaging flow cytometers. The precision of the neural network image classification was investigated through the morphological classification of specific cell types in a heterogeneous cellular population, where cell type could not be assessed via measuring the cell size. Our experiments confirm that the sIFC platform was able to successfully classify Jurkat and EL4 cells within a mixture on the basis of morphological differences. Additionally, the platform has a simple hardware configuration, comprising only a smartphone, homemade bright-field optics, and a microfluidic device. As shown in Table S1, the cost of all of the components used to construct the sIFC was €1376. Key features of the platform include the ability to perform real-time, label-free, and high-resolution cellular analysis using sheathless flows. Due to these aforementioned characteristics, we expect that the sIFC will significantly contribute to the progress of IFC in the field of single-cell, point-of-care diagnostics. The current system is 15 cm × 25 cm × 25 cm in size. However, it can be further miniaturized into an even more compact optical framework by including smaller lenses

and custom 3D-printed parts. Additionally, a small-footprint piezo pump can be used for sample injection. System performance with respect to the real-time throughput can also be improved by using a cloud-based system and a dedicated GPU for data and image processing. Finally, we expect that the sIFC platform can readily be adapted for use in resource-limited settings. The app may be converted to an open-source version, which would allow customization for different diagnostic applications.

■ ASSOCIATED CONTENT

SI Supporting Information

The Supporting Information is available free of charge at <https://pubs.acs.org/doi/10.1021/acs.analchem.3c03213>.

Additional experimental details, including information about the deep learning model used for cell image classification and the smartphone application. Additional figures, including the optical resolution of the sIFC platform, the image-processing pipeline, examples of in-focus and out-of-focus images acquired using the sIFC platform, and details of the field of view of the system, along with its corresponding throughput. An additional table describes the prices of the optomechanical components of the sIFC platform (PDF)

■ AUTHOR INFORMATION

Corresponding Authors

Stavros Stavrakis – Institute for Chemical and Bioengineering, ETH Zurich, 8093 Zürich, Switzerland; orcid.org/0000-0002-0888-5953; Email: stavros.stavrakis@chem.ethz.ch

Andrew J. deMello – Institute for Chemical and Bioengineering, ETH Zurich, 8093 Zürich, Switzerland; orcid.org/0000-0003-1943-1356; Email: andrew.demello@chem.ethz.ch

Authors

Mahmut Kamil Aslan – Institute for Chemical and Bioengineering, ETH Zurich, 8093 Zürich, Switzerland

Yun Ding – Institute for Chemical and Bioengineering, ETH Zurich, 8093 Zürich, Switzerland; orcid.org/0000-0002-7784-7758

Complete contact information is available at: <https://pubs.acs.org/doi/10.1021/acs.analchem.3c03213>

Author Contributions

M.K.A. performed the experimental work. M.K.A. and Y.D. were responsible for the image data analysis. M.K.A. developed the Android application. M.K.A., S.S., and A.J.dM. wrote the manuscript and conceptualized the project. S.S. and A.J.dM. supervised the project.

Notes

The authors declare no competing financial interest.

■ ACKNOWLEDGMENTS

This work was supported by the Strategic Focus Area Advanced Manufacturing: Microfluidics Grant and ETH Zurich.

■ REFERENCES

- (1) Hur, S. C.; Tse, H. T. K.; Di Carlo, D. *Lab Chip* **2010**, *10*, 274–280.
- (2) McKinnon, K. M. *Curr. Protoc. Immunol.* **2018**, *120* (1), S.1.1–S.1.11.
- (3) Fan, Y.-J.; Hsiao, Y.-C.; Weng, Y.-L.; Chen, Y.-H.; Chiou, P.-Y.; Sheen, H.-J. *Sens. and Actuators B Chem.* **2020**, *320*, No. 128255.
- (4) Hong, B.; Zu, Y. *Theranostics* **2013**, *3* (6), 377–394.
- (5) Knijnenburg, T. A.; Roda, O.; Wan, Y.; Nolan, G. P.; Aitchison, J. D.; Shmulevich, I. *Mol. Syst. Biol.* **2011**, *7*, 531.
- (6) Marrone, B. L. *SLAS Technol.* **2009**, *14* (3), 148–156.
- (7) Park, Y.; Abihssira-García, I. S.; Thalmann, S.; Wiegertjes, G. F.; Barreda, D. R.; Olsvik, P. A.; Kiron, V. *Front. Immunol.* **2020**, *11*, 203.
- (8) Basiji, D. A.; Ortyu, W. E.; Liang, L.; Venkatachalam, V.; Morrissey, P. *Clin. Lab. Med.* **2007**, *27* (3), 653–668.
- (9) Rane, A. S.; Rutkauskaitė, J.; deMello, A.; Stavrakis, S. *Chem.* **2017**, *3* (4), 588–602.
- (10) Miura, T.; Mikami, H.; Isozaki, A.; Ito, T.; Ozeki, Y.; Goda, K. *Biomed. Opt. Express* **2018**, *9* (7), 3424–3433.
- (11) Holzner, G.; Mateescu, B.; van Leeuwen, D.; Cereghetti, G.; Dechant, R.; Stavrakis, S.; deMello, A. *Cell Rep.* **2021**, *34* (10), No. 108824.
- (12) Ottesteanu, C. F.; Ugrinic, M.; Holzner, G.; Chang, Y.-T.; Fassnacht, C.; Guenova, E.; Stavrakis, S.; deMello, A.; Claassen, M. *Cell Rep. Methods* **2021**, *1* (6), No. 100094.
- (13) Statista. *Number of smartphone mobile network subscriptions worldwide from 2016 to 2022, with forecasts from 2023 to 2028.* <https://www.statista.com/statistics/330695/number-of-smartphone-users-worldwide/> (accessed 2023-05-27).
- (14) Udrea, A.; Mitra, G. D.; Costea, D.; Noels, E. C.; Wakkee, M.; Siegel, D. M.; de Carvalho, T. M.; Nijsten, T. E. C. *J. Eur. Acad. Dermatol. Venereol.* **2020**, *34* (3), 648–655.
- (15) Freeman, K.; Dinnes, J.; Chuchu, N.; Takwoingi, Y.; Bayliss, S. E.; Matin, R. N.; Jain, A.; Walter, F. M.; Williams, H. C.; Deeks, J. J. *BMJ* **2020**, *368*, m127.
- (16) Ruppert, C.; Phogat, N.; Laufer, S.; Kohl, M.; Deigner, H.-P. *Microchim. Acta* **2019**, *186* (2), 119.
- (17) Xiao, W.; Huang, C.; Xu, F.; Yan, J.; Bian, H.; Fu, Q.; Xie, K.; Wang, L.; Tang, Y. *Sens. and Actuators B: Chem.* **2018**, *266*, 63–70.
- (18) Colombo, M.; Bezinge, L.; Rocha Tapia, A.; Shih, C.-J.; de Mello, A. J.; Richards, D. A. *Sens. Diagn.* **2023**, *2* (1), 100–110.
- (19) Ji, D.; Liu, L.; Li, S.; Chen, C.; Lu, Y.; Wu, J.; Liu, Q. *Biosens. and Bioelectron.* **2017**, *98*, 449–456.
- (20) Ji, D.; Liu, Z.; Liu, L.; Low, S. S.; Lu, Y.; Yu, X.; Zhu, L.; Li, C.; Liu, Q. *Biosens. and Bioelectron.* **2018**, *119*, 55–62.
- (21) Pramanik, H. S.; Pal, A.; Kirtania, M.; Chakravarty, T.; Ghose, A. Ch 16: Smartphone-Based Sensors in Health and Wellness Monitoring—Perspectives and Assessment of the Emerging Future. In *Smartphone-Based Detection Devices*; Hussain, C. M., Ed.; Elsevier, 2021; p 375–398.
- (22) Im, H.; Castro, C. M.; Shao, H.; Liong, M.; Song, J.; Pathania, D.; Fexon, L.; Min, C.; Avila-Wallace, M.; Zurkiya, O.; Rho, J.; Magaoy, B.; Tambouret, R. H.; Pivovarov, M.; Weissleder, R.; Lee, H. *Proc. Natl. Acad. Sci. U. S. A.* **2015**, *112* (18), 5613–5618.
- (23) de Haan, K.; Ceylan Koydemir, H.; Rivenson, Y.; Tseng, D.; Van Dyne, E.; Bakic, L.; Karincin, D.; Liang, K.; Ilango, M.; Gumustekin, E.; Ozcan, A. *npj Digit. Med.* **2020**, *3* (1), 76.
- (24) Zhu, H.; Mavandadi, S.; Coskun, A. F.; Yaglidere, O.; Ozcan, A. *Anal. Chem.* **2011**, *83* (17), 6641–6647.
- (25) Holzner, G.; Stavrakis, S.; deMello, A. *Anal. Chem.* **2017**, *89* (21), 11653–11663.
- (26) Donnenberg, A. D.; Meyer, E. M. *Clinical Immunology Newsletter* **1999**, *19* (10), 125–128.
- (27) Chang, W.-J.; Chen, L.-B.; Hsu, C.-H.; Lin, C.-P.; Yang, T.-C. *IEEE Access* **2019**, *7*, 44441–44458.
- (28) Lu, J.; Behbood, V.; Hao, P.; Zuo, H.; Xue, S.; Zhang, G. *Knowl. Based Syst.* **2015**, *80*, 14–23.